Silicon-Based Anodes for Li Batteries: Thermodynamics, Structural Analysis, and Li Diffusion

Marco Fronzi,*,†,‡ Amanda Ellis,† and Eirini Goudeli*,†

†*School of Chemical Engineering, University of Melbourne, Parkville VIC 3010, Australia*

‡*School of Mathematics and Physics, University of Technology Sydney, Broadway, NSW 2007, Australia*

E-mail: marco.fronzi@unimelb.edu.au; eirini.goudeli@unimelb.edu.au

Abstract

Quantum mechanical and machine learning models are used to analyze the properties of silicon composite materials and their impact on lithium-ion batteries' anode performance. The analysis focuses on addressing challenges related to significant volume expansion during lithiation and provides valuable insights into the Gibbs free energy, chemical potentials, and relative stability of Li^0 and Li^+ species. Furthermore, the study explores how Li^+ ions behave in both the primary and secondary phases of the anode, assessing the impact of their formation on ion diffusion. This work highlights the fundamental significance of secondary phases in shaping micro-structural features that impact anode properties, elucidating their contribution to the Li diffusion pathway tortuosity, which is the primary cause for the fracture of Si anodes in Li−ion batteries.

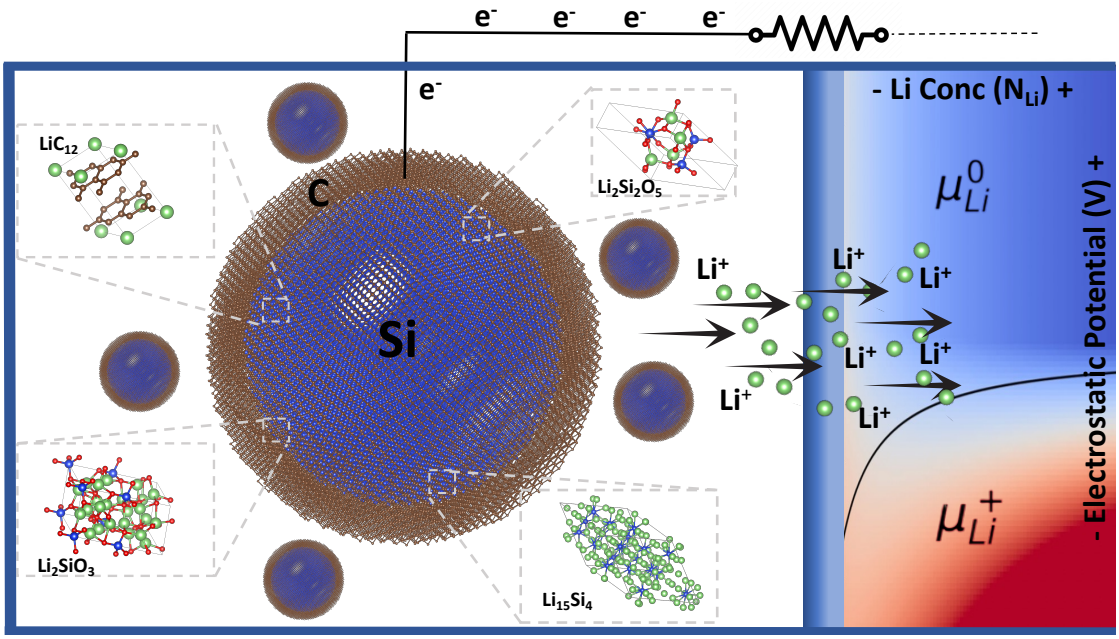

Lithium-ion batteries (LIBs) are the most commonly used energy storage devices in portable electronics, electric vehicles, and renewable energy systems due to their high energy density and lack of memory effect.[1–3] During charge and discharge cycles, the anode plays a crucial role by storing and releasing lithium (Li^+) ions, facilitating energy storage in LIBs.[4] Silicon composites have received considerable attention as potential anode materials for LIBs due to their high theoretical capacity, low delithiation voltage, low cost, and abundance.[5] However, rapid capacity decay and short life-cycle make the application of Si anodes challenging.[6,7] Large volume expansion of Si upon lithiation results in mechanical stress, fragmentation, and loss of electrical contact, contributing to the degradation of the anode itself and reducing the Solid Electrolyte Interphase (SEI) life cycles.[8–10] The SEI life span and the overall anode stability are also significantly affected by lithium-ion diffusion. Both simulations and experiments indicate that the high stress induced by the Li concentration gradient and the consequent anisotropic deformation is the primary cause of fracture in Si particles, and a direct link between Li diffusion and crystal microstructure, exists, highlighting the interplay between Li diffusion, internal microstructures, and fracture mechanics.[2,11] Therefore, uneven lithium diffusion, along with unfavorable structural properties, can lead to an unstable SEI layer and compromise the anode, accelerating battery degradation.[2,11,12] [13,14]

In this context, secondary phases could serve as SEIs, and depending on their specific structural properties, they can either intensify or mitigate the impact of volume changes.[15,16] Furthermore, lithium plating occurs when Li^+ ions are deposited onto the anode surface as metallic lithium, instead of being inserted into the anode material. This usually arises from rapid charging, which forces Li^+ ions to reach the anode faster than they can be inserted.[17–19] Understanding lithium diffusion can help to prevent lithium plating by guiding the design of anode materials and charging protocols that ensure the appropriate rate of Li^+ ion insertion. Furthermore, identifying secondary phases that may unbalance the diffusion through the anode is crucial for the design of high-performance LIBs.[7,20,21]

Carbon-coated silicon ($Si - C$) composites have been suggested as a solution to these

problems. The carbon layer in these composites can alleviate volume changes, reducing the stress on Si particles and preserving their structural integrity.[22,23] It also provides an electrically conductive network that maintains electrical connectivity even if Si particles fracture, and acts as a barrier between Si and the electrolyte, reducing the formation of an unstable SEI layer. This, in turn, improves the battery capacity retention and coulombic efficiency.[24,25] However, understanding the complex interplay between these mechanisms and their effect on anode performance is still limited.[26–29] Secondary phases also play a crucial role as micro-structural features that significantly influence anode properties and contribute to the tortuosity of the Li pathway, which is a primary factor behind anisotropic lithiation, the major cause of Si anode fracture in LIBs.[30–32]

Here, a comprehensive analysis of secondary phase exploration is presented, including their relative stability, structural properties, and Li^+ ion diffusion. The mechanical and thermodynamic properties of anodic materials are calculated by means of density functional theory, where potentially stable secondary phases are selected using machine learning (ML) models. *Ab-initio* molecular dynamics (AIMD) is carried out to investigate the Li diffusion in selected Si, C, Li, and O secondary phases.

The properties of pristine and lithiated Si cells were calculated for a (2×2×2) cubic crystalline Si (c−Si) containing 64 Si atoms, followed by insertion of Li atoms in interstitial vacuum regions of the crystal structure in their minimum energy configuration. The Li concentration was varied from 0% to ∼12.5% of the maximum reported capacity (Si/Li ∼ 1/4), corresponding to 32 interstitial Li atoms, ensuring that our model reproduces lithiation in the linear regime.[33] The formation energy of neutral lithium (Li^0) in relation to its concentration (∼1% to 50%) falls within 0.35-1.22 eV, indicating that Li^0 formation is less favourable at lower concentration, consistently with the literature.[34,35] The formation energy of positively charged lithium (Li^+) is determined by: $E_{Li^+} = E_{Li^0} + \mu_{Li^0} + q\mu_e$.[36,37] The silicon super-cell volume was optimized by evaluating the energy change in response to volume alterations (Table 1 and Figure 1a), using the Murnaghan equation (see SI Eq. 1). The results confirm

strong dependence of the volume energy on the concentration of Li atoms.[38]

Table 1: Supercell volume and its change upon lithiation (neutral and positively charged). Data is reported in absolute values and as percentage calculated with respect to the pristine Si cell. The compositions include Si with 0, 1, 2, 16 or 32 interstitial Li^0 and Li^+.

Comp	Cell Vol (A^3)	Vol Change (%)
Si_{64}	1286.8284	0.00
Si_{64}-Li^0_1	1294.9273	0.62
Si_{64}-Li^0_2	1303.1305	1.28
Si_{64}-Li^0_{16}	1416.9113	10.10
Si_{64}-Li^0_{32}	1530.9512	18.97
Si_{64}-Li^+_1	1274.2081	-0.98
Si_{64}-Li^+_2	1261.8059	-1.94
Si_{64}-Li^+_{16}	1123.7325	-12.66
Si_{64}-Li^+_{32}	1016.5804	-21.00

A higher amount of Li interstitials causes significant distortion of the Si lattice and a subsequent increase in volume. The inclusion of a single Li^0 interstitial atom triggers a 0.62% expansion of the Si supercell, which can be attributed to the spatial rearrangement induced by the Li atom occupying the interstitial site in the lattice. The volume expansion increases almost linearly up to 50% occupation of the total available interstitial sites, suggesting no phase transition within this concentration range. In contrast, introduction of Li^+ ions induces volume decrease, which is proportional to lithium concentration. This trend likely reflects an electrostatic attraction between the positively charged interstitial sites and the electrons within the Si lattice, reducing the interatomic distances, and leading to anode structural degradation, which is a crucial issue in the design of LIBs.[38] The electrostatic potential difference between the lithiated and delithiated cells, used as reference in the chemical potential formulation, was estimated by calculating the charge density averaged across the three spatial dimensions (see SI Eq. 7 for details), as shown in Table 2 and Figure 1b.

The electrostatic potential in Li−Si cells decreases with increasing Li^+ ion concentration, while ΔV increases. This increasing ΔV can significantly affect the mobility of charged species within the cell, affecting the cell's capacity and energy efficiency. To investigate the

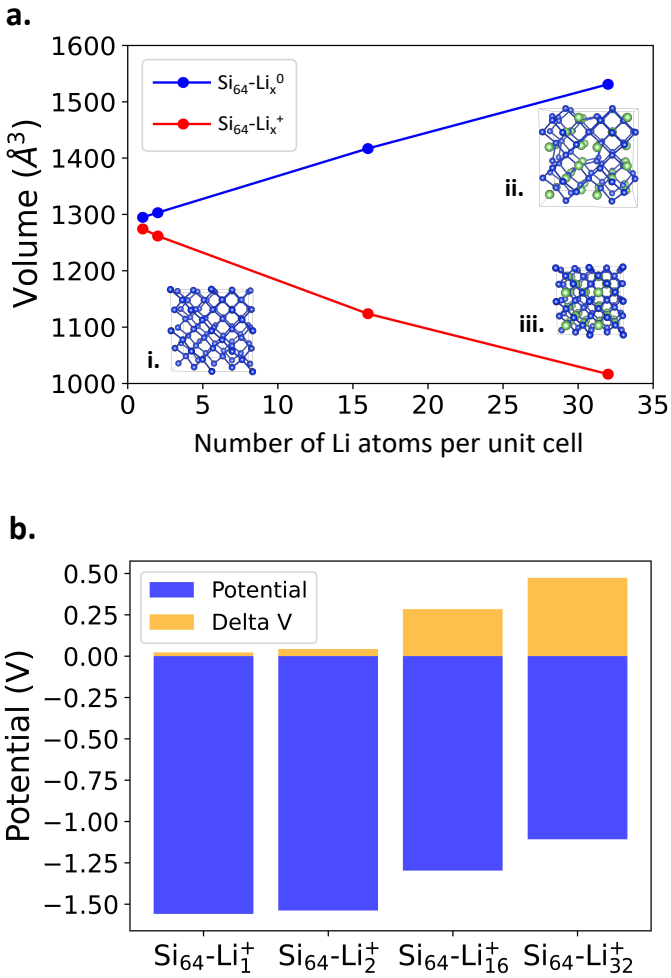

Figure 1: a) Si_{64} supercell volume change upon lithiation. The number of Li^0 (blue) and Li^+ (red) has been added to the interstitial sites to reach a Li/Si ratio of 1/2. In the figure, i., ii. and iii. Show the pristine and lithiated cubic Si_{64} cells, using neutral and positive Li, respectively. Li and Si atoms are depicted in green and blue, respectively. b) Electrostatic potential in $Si_{64} - Li^+$ cells calculated per Li^+ concentration with respect to the Si cell.

Table 2: Electrostatic potential in Si_{64}-Li^+ cells calculated per Li^+ concentration with respect to the Si_{64} cell. All the quantities are normalized per atom.

Cell	Potential (V)	ΔV (V)	ΔV (V/Å^3)
Si_{64}-Li^+_1	-1.5591	0.0223	1.7546×10^{-5}
Si_{64}-Li^+_2	-1.5384	0.0431	3.4135×10^{-5}
Si_{64}-Li^+_{16}	-1.2970	0.2845	2.5317×10^{-4}
Si_{64}-Li^+_{32}	-1.1076	0.4739	4.6613×10^{-4}

relative thermodynamic stability of the Si and Li−Si systems, with respect to the secondary phases, the Gibbs free energy is calculated as a function of Li concentration, charge, and temperature (see Thermodynamics section of the SI). Figure 2a shows the Gibbs free energy with the volume change, revealing that the positively charged, lithiated cells are the most stable and the delithiated cell is the least stable, with energies equal to -5.38, -9.01 and -5.62 eV/atom for the Si_{64}, $Si_{64}-{Li^+}_{32}$ and $Si_{64}-{Li^0}_{32}$, respectively. Li charge state change leads to a 9.3×10^{-2} eV Gibbs free energy decrease per Li atom, indicating a more stable configuration in its positive charge state. The $Si_{64}-{Li^0}_{32}$ cell exhibits moderate thermodynamic stability, suggesting that the incorporation of Li^0 atoms enhances system stability compared to the pure silicon configuration. However, this enhancement is not as significant as that observed with Li^+, confirming the inherent propensity of the cell to discharge as it naturally evolves towards a higher stability state.

To analyse the stability of Li^0 and Li^+, we calculated the chemical potentials as a function of the electrostatic potential and Li concentration (Figure 2b), as described by Eq. 9 in the SI. At low Li concentrations, the chemical potential μ_{Li^+} stabilizes at positive electrostatic potential, suggesting that a non-zero driving force is required to extract Li^+ ions, and indicating a non-linear relationship between Li concentration and charge/discharge rate.

This observation aligns with the lower chemical potential of Li^+, which indicates stability versus the neutral state for a larger elecrrochemical potential range. Therefore, the formation of Li^0 is less probable during the linear expansion/contraction range. Our results support the conclusion of Prener *et al.* that, in their experimental paper report how "a possible nonlinear region in volume expansion can be due to the precipitation of lithium metal", and suggest

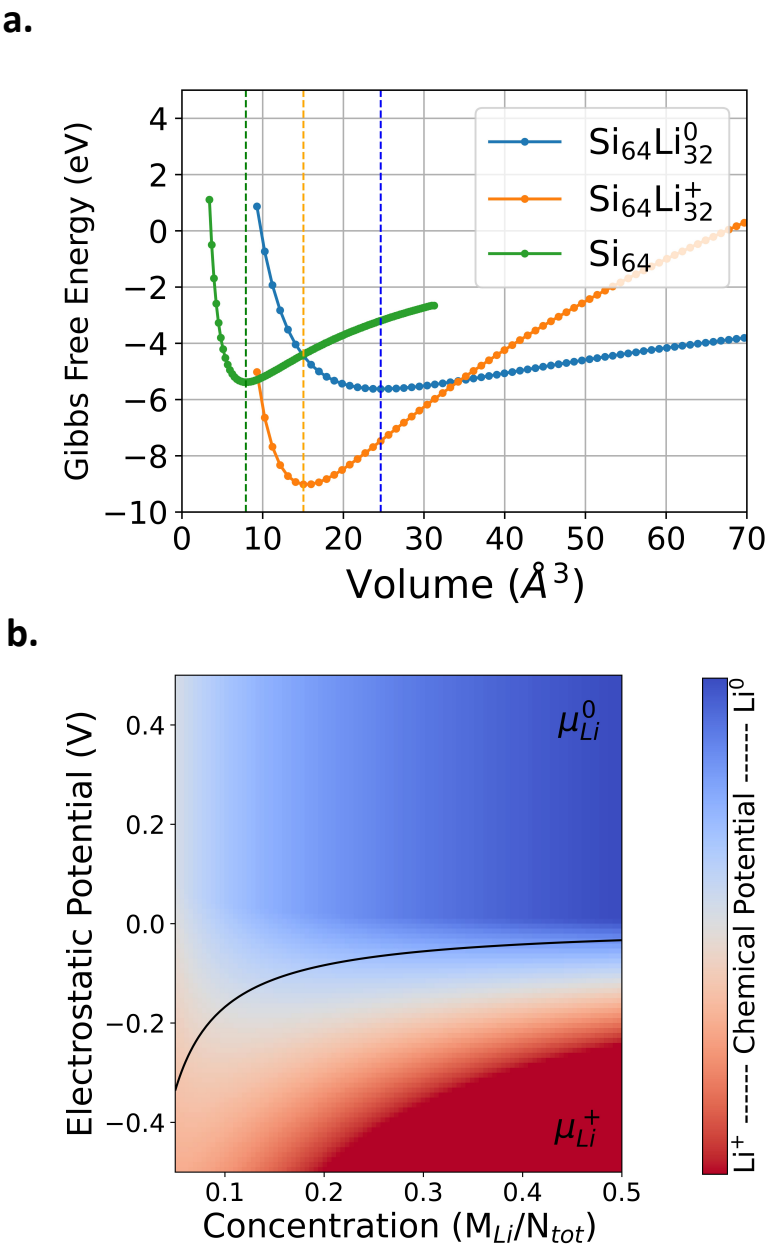

Figure 2: a) Gibbs free energy calculated for the Si_{64} supercell that include interstitial Li atoms in their neutral and charge state (Li^0 and Li^+). All the quantities are normalized per atom. b) The contour plot is a 2D representation of μ_{Li^0} and μ_{Li^+} relative stability at each point in the concentration-electrostatic potential plane. The areas corresponding to Li^0 and Li^+ relative stability is depicted in blue and red, respectively. Colors indicate whether, in a 3D space plot, Li^0 or Li^+ energy surfaces have the lowest value.

how to reduce precipitation by controlling the electrostatic potential .[39]

To estimate Li mobility, the diffusion coefficient has been calculated from the AIMD-obtained autocorrelation function (see Eq. 10 in the SI), as shown in Table 3.[40] The diffusion coefficients are in line with those measured using cyclic voltammetry, electrochemical impedance spectroscopy and galvanostatic intermittent titration measurements (ranging from $\sim 10^{-13}$ to $\sim 10^{-12}$ cm^2/s), calculated by kinetic Monte Carlo calculations (1.38×10^{-13} cm^2/s), and within the values calculated by AIMD 4.92×10^{-14} cm^2/s and 1.05×10^{-11} cm^2/s.[41–43] The diffusion coefficient of Li^+ decreases with increasing lithium concentration, indicating that diffusion becomes increasingly hindered as the electrode becomes more lithiated, due to the scarcity of available interstitial sites upon near full capacity.

This result could assist the development of more accurate mathematical modelling of the LIB state of charge by providing reliable chemical potential and diffusivity values as well as boundary conditions. This information can be incorporated into differential equations that describe electrochemical processes within the battery that are used for estimating the state of charge of LIBs, which is crucial for battery management systems.[44–46]

Interestingly, Li^+ shows significantly reduced mobility due to the formation of $Li^+ - Li^+$ bonding states confirmed by Crystal Orbital Overlapping Population analysis (see Fig. S3). which could lead to local structural changes in the silicon lattice, potentially contributing to the mechanical stress and strain observed during lithiation. The exothermic nature of lithiation, coupled with the reduced mobility of Li^+ ions, suggests that thermal management could be a critical aspect of battery design. The heat generated during lithiation needs to be effectively dissipated to prevent thermal runaway and ensure the safety and longevity of the battery. Furthermore, the analysis of the chemical potentials confirms the preferential flow of Li^+ ions during charge/discharge and suggests possible lithium plating at low lithium concentrations.

To explore the formation and influence of secondary phases we examine the possible crystals in the presence of Li, Si, C, and O, which are present in the Si−C anodes (e.g.,

Table 3: Lithium diffusion Coefficient (D_{Li}) in 64 atoms cell c−Si, calculated at different Li concentration and charge states.

Li	D_{Li} (cm^2/s)
Li_1^0	2.15×10^{-12}
Li_2^0	1.78×10^{-12}
Li_{32}^0	1.10×10^{-12}
Li_1^+	3.82×10^{-12}
Li_2^+	6.32×10^{-13}
Li_{32}^+	7.53×10^{-13}

C−coated Si).[47,48] Ideally, secondary phases should exhibit good elasticity and Li mobility comparable to Si, to achieve enhanced overall anode elasticity and prevent unbalanced diffusion. This would help mitigate the SEI degradation caused by the volumetric expansion of Si, preserving Li mobility, and preventing imbalanced Li diffusion through the anode that could lead to lithium plating. The bulk modulus and shear modulus are key quantities for quantifying the mechanical properties, reflecting the material resistance to volume change under compression, and characterizing ductility, brittleness, and hardness at micro-scale. Hardness and brittleness are correlated due to strong atomic bonds and rigid crystal structure in hard materials, making them prone to fracture rather than plastic deformation.[49–52] While these correlations are not strict rules, in the analysis of micro-structural properties of crystals, bulk and shear moduli can serve as indicators of elasticity, hardness, and brittleness within the crystal micro-structures of anodic phases.

Accounting for Si, Li, C and O elements near the Si−C anode interface, a total of 625 crystal structures were generated by exploring all possible combinations and arrangements within each space group and crystal lattice. Statistical information regarding these structures is reported in Figure 3. Interestingly, the Cmcm space group is the most prevalent among these structures, and the dominant lattice constant is comparable to that of c−Si.

Utilizing Magpie feature engineering and Random Forest models, we predicted the elastic properties of the secondary phases, characterized by the bulk modulus (K_{VRH}) and shear modulus (G_{VRH}). The model robustness and predictive power are confirmed by the metrics

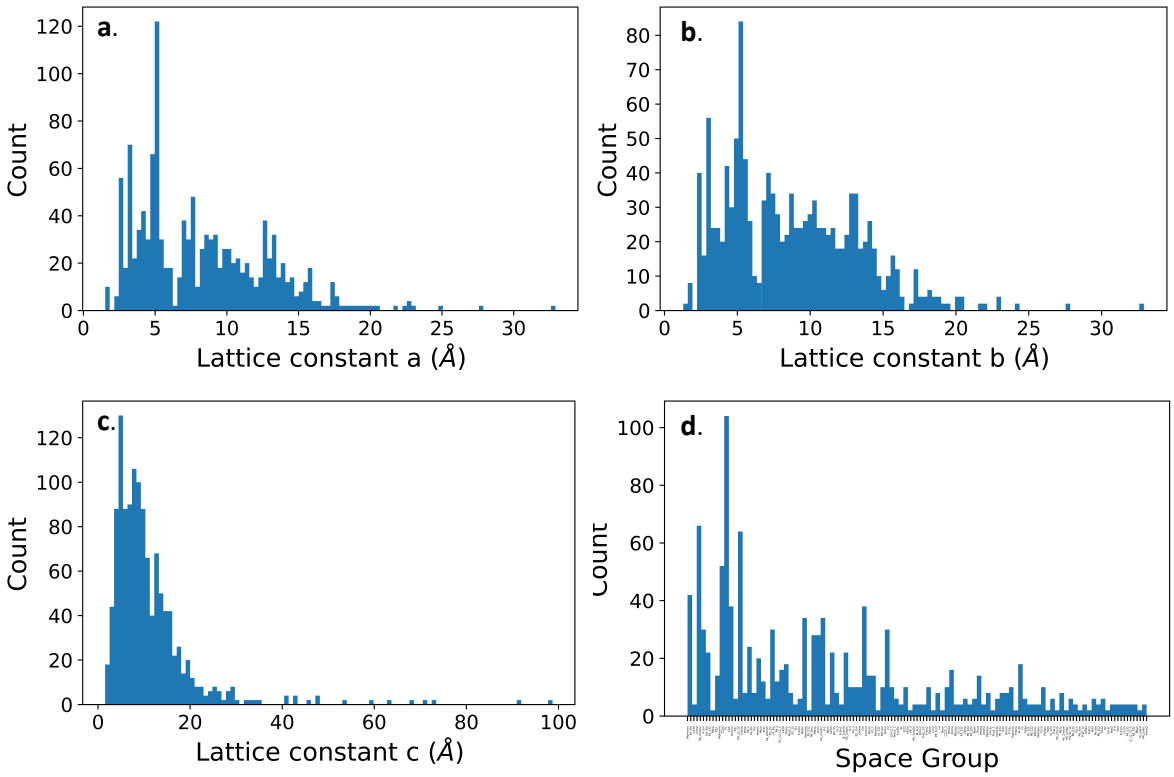

Figure 3: Statistical distributions of secondary phases structural parameters. a), b) and c) panels show the Lattice constants, whereas panel d) shows the Space Group distribution of the Si-Li-C-O secondary phases.

values reported in the SI. The predicted bulk modulus ranges from ∼16 to ∼300 GPa, while the shear modulus ranges from ∼72 to ∼350 GPa. For comparison, the bulk and shear moduli of c−Si are ∼92 GPa and ∼60 GPa, respectively. Figure 4c displays the distribution of these values, with a comprehensive list provided in the SI. The calculated Pearson coefficient is P = 0.916, indicating a strong linear correlation between the bulk and shear moduli in Si-Li-C-O crystals, which has repercussions on the micro-structural brittleness and hardness, as mentioned earlier.

The strong linear correlation between shear and bulk moduli allows the analysis of element-fraction/crystal-symmetry-elasticity correlations by using only bulk modulus values (see Figs. 4a and 4b). Random Forest models are used to estimate these correlations, with carbon marked as vital for predicting elastic properties. Carbon's predominance over other elements (C=0.79, Si=0.18, O=0.03 and Li=0.02) and a Pearson coefficient of 0.68 suggest a moderate correlation between carbon fraction and micro-hardness.

From the complete database, stable phases were isolated, and their Gibbs free energy was computed (see SI Eq. 2). The Gibbs energy trend as a function of the volume is shown in Figure 4d and the minima are reported in Table 4. Interestingly, the volume per atom for the secondary phases spans approximately 18 to 26 A3/atom, which is close to the volume of the lithiated Si cell. Additionally, the diffusion coefficients of interstitial Li^0 and Li^+ were computed employing AIMD at 300 K. For these calculations, each cell was expanded to ensure a Li dilution of approximately 1/40 host-cell-atoms to avoid Li^+-Li^+ interactions, described previously in a Si_64 cell. Consequently, the Li diffusion data in secondary phases can be compared with data in the Si cell under diluted conditions (i.e., a single atom per Si cell). The coefficients are reported in Table 4, which summarizes all the relevant calculated properties of possible secondary phases.

Considering the whole set of structures, a Pearson correlation coefficient has been calculated between the diffusion coefficient and variables such as crystal density, as well as Li, Si, O, and C concentrations corresponding to -0.048, 0.147, -0.028, 0.971, and 0.250,

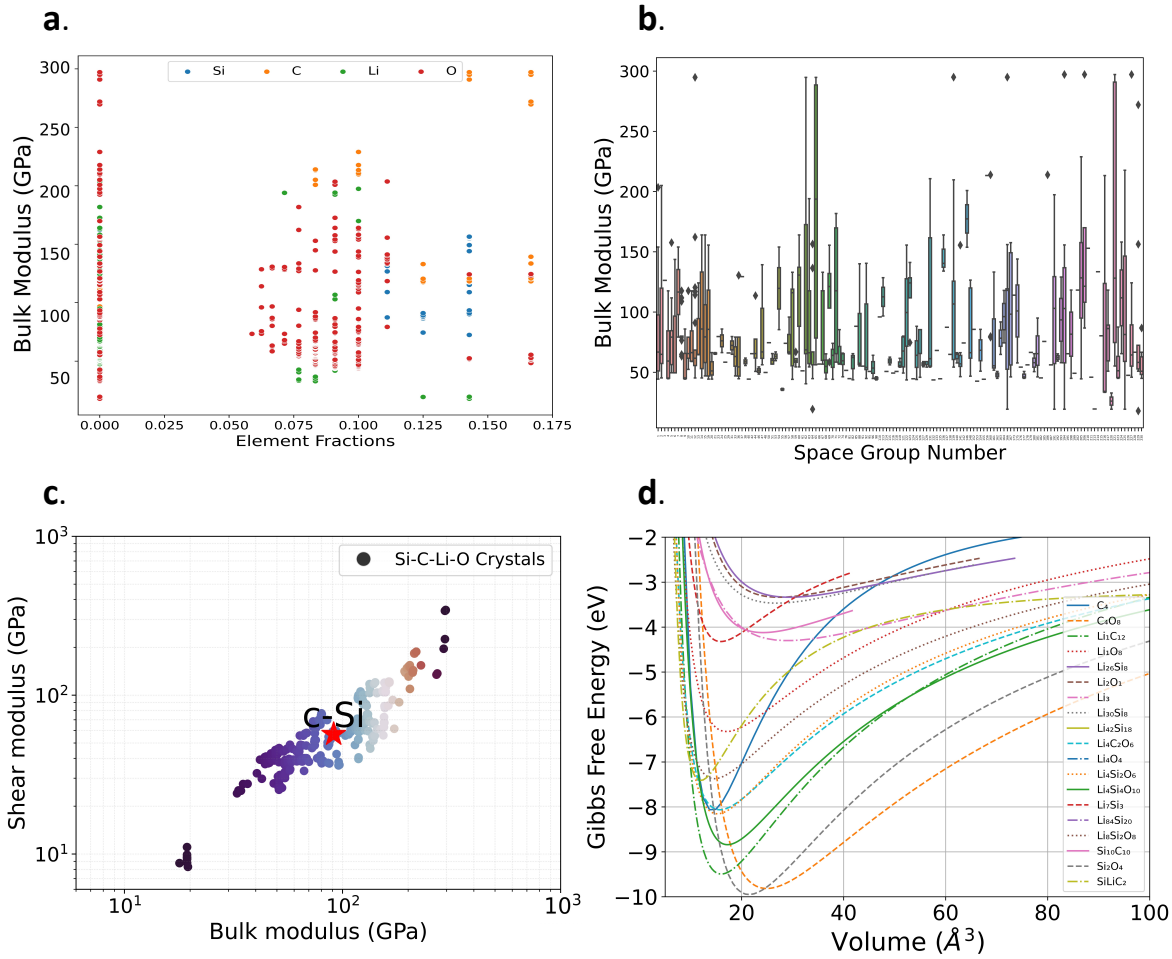

Figure 4: a) Bulk modulus relationship with crystals element fraction. Each element is represented by a scatterplot. b) Space group number vs bulk modulus distribution in secondary phases. Each box in the plot represents the distribution of bulk modulus values for a specific space group. The box shows the interquartile range (IQR), which spans from the 25th percentile (lower edge of the box) to the 75th percentile (upper edge of the box). The horizontal line inside the box represents the median value. The whiskers extend from the edges of the box to show the range of the data excluding outliers. Any points outside the whiskers are considered outliers and plotted individually as dots. Colours here are included only to facilitate the identification of different lines. c) Distribution of bulk and shear moduli of the secondary phases. The red star indicates the cubic silicon values location. Color scale qualitatively indicates the micro-structural hardness, dividing the set into seven microhardness groups. d) Gibbs free energy of the stable secondary phases. Energies and volumes are normalized per number of atoms in each crystal cell.

respectively, indicating a very strong linear correlation between the diffusion coefficient and O concentration. Although the number of samples considered in this analysis might not be statistically significant, they provide valuable insights for future research in this area.

Table 4: This table presents the diffusion coefficients of interstitial Li (D_{Li^0}) and Li^+ (D_{Li^+}) in cm^2/s calculated by AIMD, along with their corresponding Space Group (Hermann-Maguin notation), bulk modulus (K_{VRH}) and shear modulus (G_{VRH}) given in GPa calculated using random forest models and Gibbs free energies (normalized per atom number) calculated using Eq. 2 and 3 described in the SI.

Crystal	Space Group	D_{Li^0} (cm^2/s)	D_{Li^+} (cm^2/s)	K_{VRH} (GPa)	G_{VRH} (GPa)	E_{Gibbs} (eV/atom)
C_4	R$\bar{3}$m	7.47×10^{-13}	9.36×10^{-13}	117.98	94.89	-8.06
C_4O_8	Pa$\bar{3}$	1.77×10^{-12}	7.25×10^{-14}	138.54	51.80	-9.81
Li_1O_8	Cm	7.91×10^{-12}	1.23×10^{-11}	192.43	141.36	-6.32
Li_2O_1	Fm$\bar{3}$m	5.70×10^{-12}	1.83×10^{-12}	36.69	27.67	-3.50
Li_4O_4	P6$_3$/mmc	8.91×10^{-13}	5.56×10^{-13}	127.05	71.06	-3.33
Li_3	R$\bar{3}$m	8.02×10^{-12}	1.16×10^{-11}	68.24	57.88	-4.29
Li_1C_{12}	P6/mmm	1.91×10^{-11}	7.20×10^{-11}	75.61	62.19	-9.49
$Li_4C_2O_6$	C2/c	7.98×10^{-13}	2.24×10^{-12}	42.65	29.77	-8.06
$Si_{10}C_{10}$	P3m1	8.45×10^{-13}	8.58×10^{-13}	73.32	68.34	-3.93
$Si_1Li_1C_2$	P4$_2$/mmc	9.52×10^{-13}	6.43×10^{-13}	43.67	38.78	-7.41
$Li_{26}Si_8$	Pbam	3.85×10^{-12}	3.56×10^{-12}	111.77	61.09	-3.35
$Li_{30}Si_8$	I$\bar{4}$3d	1.03×10^{-12}	9.11×10^{-13}	19.36	9.53	-6.79
Li_7Si_3	P3$_2$12	9.64×10^{-13}	4.98×10^{-12}	129.44	75.90	-4.32
$Li_{42}Si_{18}$	C2	9.96×10^{-13}	2.13×10^{-13}	32.82	24.10	-4.12
$Li_4Si_2O_6$	Cmc2$_1$	5.61×10^{-13}	5.04×10^{-13}	75.37	52.17	-8.15
$Li_4Si_4O_{10}$	Ccc$_2$	4.08×10^{-13}	2.88×10^{-12}	130.50	73.13	-8.84
$Li_{84}Si_{20}$	R3m	6.01×10^{-13}	2.68×10^{-12}	42.65	29.77	-7.80
$Li_8Si_2O_8$	P$\bar{1}$1	4.67×10^{-13}	7.79×10^{-13}	33.34	25.14	-7.37
Si_2O_4	I$\bar{4}$2d	7.63×10^{-13}	2.57×10^{-12}	213.35	183.00	-9.95

From the table provided, we identified:

- **Structures with Large Bulk or Shear Modulus:** The Si_2O_4 structure (I$\bar{4}$2d symmetry) has the largest bulk (K_{VRH} = 213.35 GPa) and shear modulus (G_{VRH} = 183.00 GPa).

- **Structures with Low Diffusion Coefficient:** The C_4O_8 (Pa$\bar{3}$ symmetry) structure exhibits the lowest Li^+ diffusion coefficient (7.25 $\times 10^{-14}$ cm^2/s). This, along with the correlation between carbon fraction and micro-hardness, suggests that C_4O_8 might marginally counterbalance the beneficial contribution of the carbon layer to anode

degradation.

- **Structures with low Gibbs free energy:** C_4O_8 (-9.81 eV/atom), Li_1C_{12} (-9.49 eV/atom), and Si_2O_4 (19.95 eV/atom) phases are more stable than c−Si (-9.01 eV/atom in lithiated form), indicating the irreversible formation of secondary phases. The formation of these secondary phases will contribute to anode degradation, by increasing micro-hardness, and possibly brittleness, or causing unbalanced Li^+ mobility, facilitating anode fracture formation and Li plating.

- **Structures with the Lowest Bulk and Shear Modulus and relatively large Diffusion Coefficient:** Among the analyzed structures, $Li_{30}Si_8$ ($I\bar{4}3d$ symmetry) exhibits low bulk modulus (19.36 GPa) and shear modulus (9.53 GPa), indicating favorable accommodation of volume changes during lithiation. Its Li^0 diffusion coefficient is 1.03 $\times 10^{-12}$ cm^2/s, comparable to that of c−Si. The formation of $Li_{30}Si_8$ has the potential to reduce anode degradation due to its low bulk and shear moduli and suitable lithium mobility for efficient battery operation.

The diffusion coefficient of Li^+ is 7.25×10^{-14} cm^2/s in C_4O_8 and 1.16×10^{-11} cm^2/s in Li_3, which can be regarded as the benchmark diffusion coefficient value. Ideally, diffusion coefficients should be comparable to those of Li and Li^+ in Si ($\sim10^{-12}$-10^{-13} cm^2/s) to avoid unbalanced diffusion. Also, a bulk modulus lower than that of Si ($\sim$90 GPa) is desirable to counterbalance volume charges during charge/discharge. This data provides initial insights and indications for further experimental validation and analysis to gain a deeper understanding of the fundamental mechanisms underlying the degradation of silicon-based anodes. These insights could be instrumental in guiding the design and selection of secondary phases for enhanced performance in LIBs.

The interplay between elemental composition, elasticity, and Li mobility is presented for a wide range of materials that may serve as secondary phases in Si anodes. DFT calculations confirm a significant volume change of the Si cell upon lithiation/delithiation and highlight

interstitial Li^+ as the dominant species. A non-linear transition between μ_{Li} and μ_{Li^+} at low Li concentrations indicate distinct electron-ion dynamics at different anode capacities. We propose a potential mechanism for interstitial Li^+ at high concentration, involving the formation of Li^+-Li^+ bonding states, which may reduce ion mobility at high concentration. Through thermodynamic analysis, we identify several possible stable secondary phases, including C_4O_8, Li_1C_{12}, and Si_2O_4, which exhibit greater stability compared to c−Si. A strong linear correlation is observed between bulk and shear moduli in Si-Li-C-O crystals and a moderate linear correlation between carbon fraction and micro-hardness. Formation of Si_2O_4 and Li_1C_{12} increases micro-hardness and induces unbalanced Li diffusion, contributing to anode degradation. Conversely, the formation of $Li_{30}Si_8$ enhances structural micro-elasticity without creating unbalanced Li diffusion, mitigating fracture formation and reducing anode degradation. Notably, C_4O_8 exhibits the lowest Li diffusion coefficient and high micro-hardness, suggesting that the predicted carbon-based stable secondary phases may have a detrimental effect on anode performance, counterbalancing the commonly believed benefits of carbon-based compounds in the overall silicon anode stability.

Methodology

Ab-initio calculations based on periodic DFT are used, as implemented in the Vienna *Ab-initio* Simulation Package (VASP).[53] The core and valence electron interactions were considered through the implementation of projector augmented-wave potentials, and the valence electrons were represented by periodic plane waves with a cut-off energy of 550 eV.[54,55] The pseudo-potentials of lithium were handled with a refined approach, integrating the s electron into the valence electron configuration, which improves the accuracy and reliability of treating charged states in DFT.[56] The reciprocal space was comprehensively covered by utilizing a gamma-centered k-point mesh grid.[57] The exchange-correlation functional was addressed within the framework of the generalized gradient approximation, as in the Perdew, Burke,

and Ernzerhof (PBE) formulation.[58] Molecular Dynamics (MD) simulations were carried out in a canonical ensemble at 300 K.[59] ML models were integrated with DFT calculations to extrapolate the bulk and shear modulus of a large number of crystals resulting from the combination of selected elements. The employed ML models that were selected are suitable for handling high-dimensional data and capturing complex relationships between input features and target properties. Materials Agnostic Platform for Informatics and Exploration (magpie) featurization has been used to enable efficient comparison and analysis of materials based on their elemental makeup.[60]

Acknowledgement

The authors would like to acknowledge the Future Batteries Industries CRC and project participants for funding the Super Anode Project. The authors would also like to acknowledge our colleagues at the University of Melbourne and CSIRO FBI CRC Super Anode project teams for their input and considered review of the report. The theoretical calculations in this research were undertaken with the assistance of resources from the National Computational Infrastructure (NCI), which is supported by the Australian Government.

Supporting Information Available

Supporting Information contains the equations used for the calculations of relevant quantities, the crystal orbital overlap population analysis, densities and relative densities of stable secondary phases, and a complete list of bulk and shear moduli calculated using ML models.

References

(1) Goodenough, J. B.; Park, K.-S. The Li-ion rechargeable battery: a perspective. *J. Am. Chem. Soc.* **2013**, *135*, 1167–1176.

(2) Wang, G.; Xu, B.; Shi, J.; Wu, M.; Su, H.; Ouyang, C. New insights into Li diffusion in Li–Si alloys for Si anode materials: role of Si microstructures. *Nanoscale* **2019**, *11*, 14042–14049.

(3) Xu, N.; Chen, T.; Lu, X.; Chen, Y.; Liu, J.; Guo, Z. Recent progress and future perspective on practical silicon anode-based lithium ion batteries. *Energy Stor. Mater.* **2020**, *26*, 153–185.

(4) He, Z.; Zhang, J.; He, X.; Yin, H.; Ji, X.; Lu, X.; Chen, L. New Si–O–C composite film anode materials for LIB by electrodeposition. *J. Mater. Chem. A* **2014**, *2*, 1727–1731.

(5) Cui, Y. Silicon anodes. *Nat. Energy* **2021**, *6*, 995–996.

(6) Liu, B.; Wang, X.; Li, Z.; Zhang, L.; Li, Y.; Li, Y.; Li, G.; Li, H. Facile and efficient fabrication of branched Si@C anode with superior cycling stability for Lithium-ion batteries. *Small* **2019**, *15*, 1803298.

(7) Prajapati, A. K.; Bhatnagar, A. A review on anode materials for lithium/sodium-ion batteries. *J. Energy Chem.* **2023**,

(8) Chen, Y.; Lu, P.; Zhang, X.; Xu, X.; Zhu, T.; Qiao, Y. Strategies for Ccntrolling or releasing the influence due to the volume change of silicon anode materials. *Materials* **2018**, *11*, 796.

(9) Ko, M.; Chae, S.; Cho, J. Challenges in accommodating volume change of Si anodes for Li-ion batteries. *ChemElectroChem* **2017**, *4*, 835–844.

(10) Song, X.; Wang, X.; Sun, Z.; Zhang, P.; Gao, L. Recent developments in silicon anode materials for high performance lithium-ion batteries. *J. Mater. Chem.* **2016**, *8*.

(11) Gao, Y.; Fan, L.; Zhou, R.; Du, X.; Jiao, Z.; Zhang, B. High-performance silicon-rich microparticle anodes for lithium-ion batteries enabled by internal stress mitigation. *Nano-Micro Lett.* **2023**, *15*, 222.

(12) Tamirat, A. G.; Lui, Y.; Dong, X.; Wang, C.; Wang, Y.; Xia, Y. Ultrathin silicon nanolayer implanted Ni_xSi/Ni nanoparticles as superlong-cycle lithium-ion anode material. *Small Struct.* **2020**,

(13) Choi, Y.-S.; Park, J.-H.; Ahn, J.-P.; Lee, J.-C. Interfacial reactions in the Li/Si diffusion couples: origin of anisotropic lithiation of crystalline si in Li–Si batteries. *Sci. Rep.* **2017**, *7*, 14028.

(14) Dreshfield, R. L. Defects in nickel-base superalloys. *JOM* **1987**, *39*, 16–21.

(15) Satalkar, M.; Kane, S. On the study of structural properties and cation distribution of $Zn_{0.75-x}Ni_xMg_{0.15}Cu_{0.1}Fe_2O_4$ nano ferrite: effect of Ni addition. *J. Phys.: Conf. Ser.* **2016**,

(16) Ye, H.; Radlińska, A. Effect of alkalis on cementitious materials: Understanding the relationship between composition, structure, and volume change mechanism. *J. Adv. Concr. Technol.* **2017**, *15*, 165–177.

(17) Escamilla-Pérez, A. M.; Roland, A.; Giraud, S.; Guiraud, C.; Virieux, H.; Demoulin, K.; Oudart, Y.; Louvain, N.; Monconduit, L. Pitch-based carbon/nano-silicon composite, an efficient anode for Li-ion batteries. *RSC Adv.* **2019**, *9*, 10546–10553.

(18) Huang, W.; Wang, J.; Braun, M. R.; Zhang, Z.; Li, Y.; Boyle, D. T.; McIntyre, P. C.; Cui, Y. Dynamic structure and chemistry of the silicon solid-electrolyte interphase visualized by cryogenic electron microscopy. *Matter* **2019**, *1*, 1232–1245.

(19) Pang, Q.; Liang, X.; Shyamsunder, A.; Nazar, L. F. An in vivo formed solid electrolyte surface layer enables stable plating of Li metal. *Joule* **2017**,

(20) Butler, K. T.; Davies, D. W.; Cartwright, H.; Isayev, O.; Walsh, A. Machine learning for molecular and materials science. *Nature* **2018**, *559*, 547–555.

(21) Deng, Z.; Mo, Y.; Ong, S. P. Computational studies of solid-state alkali conduction in rechargeable alkali-ion batteries. *NPG Asia Mater.* **2016**, *8*, e254–e254.

(22) Ng, S.-K.; Wang, J.; Wexler, D. B.; Chew, S. Y.; Zhang, L. Amorphous Carbon-Coated Silicon Nanocomposites: A low-temperature synthesis via spray pyrolysis and their application as high-capacity anodes for lithium-ion batteries. *J. Phys. Chem. C* **2007**,

(23) Sun, W.; Hu, R.; Zhang, M.; Liu, J.; Zhu, M. Binding of carbon coated nano-silicon in graphene sheets by wet ball-milling and pyrolysis as high performance anodes for lithium-ion batteries. *J. Power Sources* **2016**,

(24) Xu, Z.; Yang, J.; Zhang, T.; Nuli, Y.; Wang, J.; Hirano, S.-i. Silicon Microparticle Anodes with Self-Healing Multiple Network Binder. *Joule* **2018**,

(25) Casimir, A.; Zhang, H.; Ogoke, O.; Amine, J. C.; Lu, J.; Wu, G. Silicon-based anodes for lithium-ion batteries: Effectiveness of materials synthesis and electrode preparation. *Nano Energy* **2016**,

(26) Dixit, M. B.; Singh, N.; Horwath, J. P.; Shevchenko, P. D.; Jones, M.; Stach, E. A.; Arthur, T. S.; Hatzell, K. B. In situ investigation of chemomechanical effects in thiophosphate solid electrolytes. *Matter* **2020**, *3*, 2138–2159.

(27) Lu, Y.; Yu, L.; Lou, X. W. D. Nanostructured conversion-type anode materials for advanced lithium-ion batteries. *Chem* **2018**, *4*, 972–996.

(28) Wu, Y.; Liu, N. Visualizing battery reactions and processes by using in situ and in operando microscopies. *Chem* **2018**, *4*, 495–520.

(29) Zhao, Y.; Amirmaleki, M.; Sun, Q.; Zhao, C.; Codirenzi, A.; Goncharova, L. V.; Wang, C.; Adair, K.; Li, X.; Yang, X. Natural SEI-inspired dual-protective layers via atomic/molecular layer deposition for long-life metallic lithium anode. *Matter* **2019**, *1*, 1215–1231.

(30) Zhu, W.; Zhou, J.; Xiang, S.; Bian, X.; Yin, J.; Jiang, J.; Yang, L. Progress of binder structures in silicon-based anodes for advanced lithium-ion batteries: a mini review. *Front. Chem.* **2021**, *9*, 712225.

(31) Provis, J. L.; Van Deventer, J. S. *Alkali activated materials: state-of-the-art report, RILEM TC 224-AAM*; 2013; Vol. 13.

(32) Su, Y.-S.; Hsiao, K.-C.; Sireesha, P.; Huang, J.-Y. Lithium silicates in anode materials for Li-ion and Li metal batteries. *Batteries* **2022**, *8*, 2.

(33) Chen, L.; Fan, X.; Ji, X.; Chen, J.; Hou, S.; Wang, C. High-energy Li metal battery with lithiated host. *Joule* **2019**, *3*, 732–744.

(34) Chou, C.-Y.; Kim, H.; Hwang, G. S. A comparative first-principles study of the structure, energetics, and properties of Li–M (M= Si, Ge, Sn) alloys. *J. Phys. Chem. C* **2011**, *115*, 20018–20026.

(35) González-Macías, A.; Salazar, F.; Miranda, A.; Trejo, A.; Hernández-Hernández, I.; Pérez, L.; Cruz-Irisson, M. Theoretical study of the mechanical and electronic properties of [111]-Si nanowires with interstitial lithium. *J. Mater. Sci.: Mater. Electron.* **2018**, *29*, 15795–15800.

(36) Björketun, M. E.; Sundell, P. G.; Wahnström, G. Structure and thermodynamic stability of hydrogen interstitials in $BaZrO_3$ perovskite oxide from density functional calculations. *Faraday Discuss.* **2007**, *134*, 247–265.

(37) Fronzi, M.; Tateyama, Y.; Marzari, N.; Nolan, M.; Traversa, E. First-principles molecular dynamics simulations of proton diffusion in cubic $BaZrO_3$ perovskite under strain conditions. *Mater. Renew. Sustain. Energy* **2016**, *5*, 14.

(38) Schiele, A.; Breitung, B.; Mazilkin, A.; Schweidler, S.; Janek, J.; Gumbel, S.; Fleischmann, S.; Burakowska-Meise, E.; Sommer, H.; Brezesinski, T. Silicon nanoparticles

with a polymer-derived carbon shell for improved lithium-ion batteries: Investigation into volume expansion, gas evolution, and particle fracture. *ACS Omega* **2018**, *3*, 16706–16713.

(39) Prener, J.; Williams, F. Effect of interstitial Li on the density of Si. *J. Chem. Phys.* **1961**, *35*, 1803–1808.

(40) Van Beijeren, H.; Kehr, K. Correlation factor, velocity autocorrelation function and frequency-dependent tracer diffusion coefficient. *J. Phys. C: Solid State Phys.* **1986**, *19*, 1319.

(41) Ding, N.; Xu, J.; Yao, Y.; Wegner, G.; Fang, X.; Chen, C.; Lieberwirth, I. Determination of the diffusion coefficient of lithium ions in nano-Si. *Solid State Ionics* **2009**, *180*, 222–225.

(42) Tritsaris, G. A.; Zhao, K.; Okeke, O. U.; Kaxiras, E. Diffusion of lithium in bulk amorphous silicon: a theoretical study. *J. Phys. Chem. C* **2012**, *116*, 22212–22216.

(43) Wang, Z.; Su, Q.; Deng, H.; He, W.; Lin, J.; Fu, Y. Q. Modelling and simulation of electron-rich effect on Li diffusion in group IVA elements (Si, Ge and Sn) for Li ion batteries. *J. Mater. Chem. A* **2014**, *2*, 13976–13982.

(44) Weppner, W. *Mater. Lithium-ion Batteries*; 2000; pp 401–412.

(45) Gao, J.; Shi, S.-Q.; Li, H. Brief overview of electrochemical potential in lithium ion batteries. *Chin. Phys. B* **2015**, *25*, 018210.

(46) Wang, N.; Xia, X.; Zeng, X. State of charge and state of health estimation strategies for lithium-ion batteries. *International Journal of Low-Carbon Technologies* **2023**, *18*, 443–448.

(47) Liu, W.-R.; Wang, J.-H.; Wu, H.-C.; Shieh, D.-T.; Yang, M.-H.; Wu, N.-L. Electrochemical characterizations on Si and C-coated Si particle electrodes for Lithium-ion batteries. *J. Electrochem. Soc.* **2005**, *152*, A1719.

(48) Liu, H.; Zhu, Z.; Yan, Q.; Yu, S.; He, X.; Chen, Y.; Zhang, R.; Ma, L.; Liu, T.; Li, M. et al. A disordered rock salt anode for fast-charging lithium-ion batteries. *Nature* **2020**, *585*, 63–67.

(49) Gorecki, T. The relations between the shear modulus, the bulk modulus and Young's modulus for polycrystalline metallic elements. *Mater. Sci. Eng.* **1980**, *43*, 225–230.

(50) Jiang, X.; Zhao, J.; Jiang, X. Correlation between hardness and elastic moduli of the covalent crystals. *Comput. Mater. Sci.* **2011**, *50*, 2287–2290.

(51) Liu, Z.; others A review of silicon-based multicomponent anode materials for lithium-ion batteries. *Energy Stor. Mater.* **2020**, *24*, 22–37.

(52) Phani, K.; Sanyal, D. The relations between the shear modulus, the bulk modulus and Young's modulus for porous isotropic ceramic materials. *Mater. Sci. Eng. A* **2008**, *490*, 305–312.

(53) Kresse, G.; Furthmüller, J. Efficiency of ab-initio total energy calculations for metals and semiconductors using a plane-wave basis set. *Comput. Mater. Sci.* **1996**, *6*, 15–50.

(54) Blöchl, P. E. Projector augmented-wave method. *Phys. Rev. B* **1994**, *50*, 17953.

(55) Payne, M. C.; Teter, M. P.; Allan, D. C.; Arias, T. A.; Joannopoulos, J. D. Iterative minimization techniques for ab initio total-energy calculations: molecular dynamics and conjugate gradients. *Rev. Mod. Phys.* **1992**, *64*, 1045.

(56) Rappe, A. M.; Rabe, K. M.; Kaxiras, E.; Joannopoulos, J. D. Optimized pseudopotentials. *Phys. Rev. B* **1990**, *41*, 1227.

(57) Monkhorst, H. J.; Pack, J. D. Special points for Brillouin-zone integrations. *Phys. Rev. B* **1976**, *13*, 5188.

(58) Perdew, J. P.; Burke, K.; Ernzerhof, M. Generalized gradient approximation made simple. *Phys. Rev. Lett.* **1996**, *77*, 3865–3868.

(59) Nosé, S. A molecular dynamics method for simulations in the canonical ensemble. *Mol. Phys.* **1984**, *52*, 255–268.

(60) Ward, L.; Agrawal, A.; Choudhary, A.; Wolverton, C. A general-purpose machine learning framework for predicting properties of inorganic materials. *npj Comput. Mater.* **2016**, *2*, 1–7.